J BONE ONCOL 45 (2024) 100599

Contents lists available at ScienceDirect

Journal of Bone Oncology

journal homepage: www.elsevier.com/locate/jbo

Research Paper

Radiomics model based on MRI to differentiate spinal multiple myeloma from metastases: A two-center study

Jiashi Cao [a,1], Qiong Li [d,1], Huili Zhang [c,1], Yanyan Wu [b,1], Xiang Wang [b], Saisai Ding [c], Song Chen [b], Shaochun Xu [b], Guangwen Duan [b], Defu Qiu [e], Jiuyi Sun [a,*], Jun Shi [c,*], Shiyuan Liu [b,*]

[a] Department of Orthopedics, Navy Medical Center, the Navy Medical University, No. 338 Huaihai West Road, Shanghai 200052, China
[b] Department of Radiology, Changzheng Hospital of the Navy Medical University, No. 415 Fengyang Road, Shanghai 200003, China
[c] School of Communication and Information Engineering, Shanghai University, 99 Shangda Road, Baoshan District, Shanghai 200444, China
[d] Department of Radiology, State Key Laboratory of Oncology in South China, Collaborative Innovation Center for Cancer Medicine, Sun Yat-sen University Cancer Center/Cancer Hospital, No. 651 Dongfeng East Road, Guangzhou 510060, China
[e] School of Information and Control Engineering, China University of Mining and Technology, Xuzhou 221116, China

HIGHLIGHTS

- The first two-center study constructing different radiomics models to differentiate spinal multiple myeloma from metastases.
- The radiomics models constructed based on MRI achieved satisfactory diagnostic performance for the classification of spinal MM and metastases.
- Radiomics models based on joint CET1 and T2WI performing better than T2WI alone, and CET1 alone.

GRAPHICAL ABSTRACT

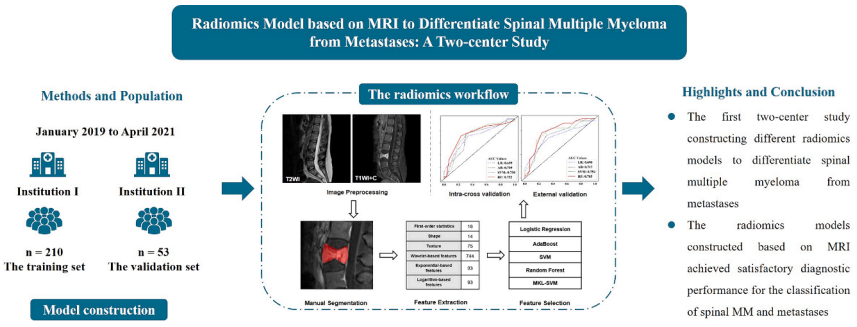

ARTICLE INFO

Keywords:
multiple myeloma (MM)
Metastases
Spine
Radiomics
Differential diagnosis

ABSTRACT

Purpose: Spinal multiple myeloma (MM) and metastases are two common cancer types with similar imaging characteristics, for which differential diagnosis is needed to ensure precision therapy. The aim of this study is to establish radiomics models for effective differentiation between them.

Methods: Enrolled in this study were 263 patients from two medical institutions, including 127 with spinal MM and 136 with spinal metastases. Of them, 210 patients from institution I were used as the internal training cohort and 53 patients from Institution II were used as the external validation cohort. Contrast-enhanced T1-weighted imaging (CET1) and T2-weighted imaging (T2WI) sequences were collected and reviewed. Based on the 1037 radiomics features extracted from both CET1 and T2WI images, Logistic Regression (LR), AdaBoost (AB), Support Vector Machines (SVM), Random Forest (RF), and multiple kernel learning based SVM (MKL-SVM) were constructed. Hyper-parameters were tuned by five-fold cross-validation. The diagnostic efficiency among different

* Corresponding authors.
E-mail addresses: sunjiuyi@smmu.edu.cn (J. Sun), junshi@shu.edu.cn (J. Shi), radiology_cz@163.com (S. Liu).
[1] Jiashi Cao, Qiong Li, Huili Zhang, and Yanyan Wu are primary authors and contributed equally.

https://doi.org/10.1016/j.jbo.2024.100599
Received 2 July 2023; Received in revised form 19 December 2023; Accepted 9 January 2024
Available online 28 March 2024
2212-1374/© 2024 The Authors. Published by Elsevier GmbH. This is an open access article under the CC BY-NC-ND license (http://creativecommons.org/licenses/by-nc-nd/4.0/).

radiomics models was compared by accuracy (ACC), sensitivity (SEN), specificity (SPE), area under the ROC curve (AUC), YI, positive predictive value (PPV), negative predictive value (NPY), and F1-score.
Results: Based on single-sequence, the RF model outperformed all other models. All models based on T2WI images performed better than those based on CET1. The efficiency of all models was boosted by incorporating CET1 and T2WI sequences, and the MKL-SVM model achieved the best performance with ACC, AUC, and F1-score of 0.862, 0.870, and 0.874, respectively.
Conclusions: The radiomics models constructed based on MRI achieved satisfactory diagnostic performance for differentiation of spinal MM and metastases, demonstrating broad application prospects for individualized diagnosis and treatment.

1. Introduction

As two types of malignant tumors commonly affecting the bone marrow, multiple myeloma (MM) and metastases are often seen as single or multiple lesions in the spine [1,2].Currently, the primary diagnosis for the two spinal malignancies relies mainly on imaging examinations. However, atypical magnetic resonance imaging (MRI) manifestations and clinical symptoms could be observed in both of spinal metastases and MM [1,3–5]. The diagnosis of MM is usually based on the measurement of quantitative serum and urine paraprotein (M protein), but some MM cases are non-secretory or hypersecretory, making diagnosis more difficult [3,6]. Although the history of the primary tumor may help the diagnosis of spinal metastasis, approximately 30% patients present with spinal metastases of unknown origin [7,8]. Differential diagnosis between spinal MM and metastases remains a challenge for radiologists, and therefore it is imperative to establish an effective method for accurate differential diagnosis between them.

MRI is generally accepted as the gold standard imaging method for assessing tumors of the spine [9,10]. It is more sensitivity in detecting lesions confined to vertebral column as compared with computer tomography (CT), standard radiography and nuclear medicine scanning [9]. However, there exists an overlap of MRI imaging manifestations between spinal MM and metastases, especially in cases with multiple vertebra focal osteolytic lesions, which may easily lead to clinical mis- or mal-diagnosis [11–13]. Although 18F-fluorodeoxyglucose positron emission tomography and CT (18F-FDG PET/CT) is vital for detecting metastasis and primary cancer, it has been demonstrated to have some disadvantages such as time-consuming, high radiation exposure and high cost for patients. Additionally, the resolution of 18F-FDG PET/CT is limited, and correlation with MRI imaging is required [3,9]. If conventional MRI could accurately predict these lesions, it would provide a beneficial, cost-effective management option for patients.

In recent years, radiomics has gained increasing attention in that it promises to reveal more biological detail and increases the spatial resolution as compared with conventional imaging methods. As a newly emerging non-invasive method, radiomics has proved to be effective in clinical diagnosis, differential diagnosis, prognosis prediction, and therapeutic effect assessment by extracting high-dimensional sets of imaging features and characterizing intratumoural heterogeneity [1,3,14]. In clinical oncology, radiomics has greatly expanded the scope of conventional medical imaging rather than focusing only on morphology. Although radiomics has made significant achievements in various types of tumors such as those originating from the lung, breast and gastrointestinal tract, studies reporting the application of MRI-based radiomics for differential diagnosis between spinal MM and metastases are limited [1,3,15–17].

The aim of this study was to develop radiomics models for differentiation between spinal MM and metastases based on MRI sequences by collecting datasets from two institutions: one for the internal training set, and the other for the external validation set. The performance of different radiomics models was assessed based on different vertebra MRI sequences, including contrast-enhanced T1-weighted imaging (CET1) alone, T2-weighted imaging (T2WI) alone, and joint CET1 with T2WI.

2. Material and methods

2.1. Patients and study design

This was a two-center retrospective study conducted at Changzheng Hospital (Shanghai, China) as Institution I, and Sun Yat-sen University Cancer Center (Guangzhou, China) as Institution II. The requirement for written informed consent was waived because of the retrospective nature of this study without any intervention on patients. Clinical characteristics and MRI sequences of patients with spinal MM or metastases were collected retrospectively, who received treatment in the two institutions from January 2019 to April 2021. The study was approved by ethics committee of each participating institution.

A total of 263 patients with spinal metastases and MM were eventually recruited from the two institutions based on the following inclusion criteria: (1) patients diagnosed with spinal MM or metastasis confirmed by histology or cellular pathology; (2) patients with preoperative MRI with qualified images, including CET1 and T2WI; and (3) patients with complete clinical information. Exclusion criterion included patients: (1) who were diagnosed with other spinal tumors; (2) who did not receive MRI scanning in our two institutions or without qualified or complete MRI images; (3) who did not undergo spine surgery or tissue biopsy without pathological findings; and (4) without complete clinical information.

Patients from Institutions I were assigned as the training set, and those from Institution II were in the external validation set, respectively. The demographic characteristics of the two cohorts are summarized in Table 1. The flowchart in Fig. 1 illustrates the analysis pathway of this study.

2.2. MRI acquisition

All patients underwent MRI examinations with General Electric Signa 1.5T (Milwaukee, USA), Philips Achieva 3.0T (Veenpluis 4-6, 5684 PC Best, the Netherlands), and Siemens Avanto 1.5T (Shenzhen,

Table 1
Clinical information for patients with spinal MM and metastases from two institutions.

Clinical factors	Training cohort (Institution I)	External cohort (Institution II)	P value
Gender			0.277
Male	132	29	
Female	78	24	
Age	57.26 ± 10.55	57.11 ± 9.51	0.921
Tumor type			0.459
MM	99	28	
Metastases	111	25	
Tumor location			0.001
Cervical vertebrae	40	1	
Thoracic vertebrae	90	17	
Lumber vertebrae	66	29	
Sacrococcygeal vertebrae	14	6	
Tumor size (cm)	4.08 ± 1.32	2.99 ± 1.75	<0.001

MM, multiple myeloma.

China). All scans were performed in a consistent manner. MRI sequences included in this study were CET1 and T2WI sequences. The adopted scanning parameters were as followed: CET1 (repetition time [TR]: 500–650 msec; echo time [TE]: 12–14 msec); T2WI (TR: 2500–4500 msec; TE: 94–120 msec); The following imaging acquisition parameters were used for both CET1 and T2WI: slice thickness, 3–6 mm; matrix ranging from 320 × 160 to 512 × 512; field of view ranging from 240 × 240 mm^2 to 380 × 380 mm^2. GD-DTPA Injection (Consun Pharma, Guangzhou, PR China) was administered intravenously using a weight-based dosing protocol of 0.2 ml/kg. Sagittal, axial and coronal images were acquired and converted to DICOM format for subsequent processes.

2.3. Lesion segmentation

All images were retrieved in the form of DICOM with accordant window width and window location from the Picture Archiving and Communication System (PACS) in both institutions. The region of interest (ROI) was manually created from sagittal CET1and T2WI using ITK-SNAP 3.8.0 software [18]. Given the possibility of multiple lesions on each patients' lumbar vertebrae, only the lesions bigger than 1 cm diameter were considered and chosen to avoid the partial volume effect. Of them, the largest was selected for the subsequent analysis. All participating radiologists were blinded to the clinical information. The ROI was outlined by one musculoskeletal radiologist with more than 5-year diagnostic experience, and the result was checked by another musculoskeletal radiologist with more than 10-year diagnostic experience. Any discrepancy between them would be solved through discussion. Both were blinded to the results of pathology, clinical information, clinical and follow-up findings. An example of ROI outline is illustrated in Fig. 2.

2.4. Feature extraction

Extracted from the ROI for each patient, a total of 1037 features were divided into 10 groups: (1) First-order statistics (n = 18), (2) shape (n = 14), (3) texture (n = 24, derived from GLCM), (4) texture (n = 16, derived from GLSZM), (5) texture (n = 16, derived from GLRLM), (6) texture (n = 14, derived from GLDM), (7) texture (n = 5, derived from NGTDM), (8) wavelet-based features (n = 744), (8) exponential-based features (n = 93), and (10) logarithm-based features (n = 93). Feature extraction was automatically conducted by the PyRadiomics package implemented in Python.

2.5. Feature selection

T-test analysis was performed for all features, which with *P* values <0.05 were selected for further analysis. Two independent sample *t* tests were used to find whether the mean and distribution of these two samples were significantly different. In the two sets of samples of normal and abnormal patients whose features involved an average, *t*-test was used to determine whether these features were significantly different. If there were significant differences, they were reserved for classification tasks, and otherwise they were removed from classification tasks. The *t*-test analysis was followed by the Lasso feature selection method, aiming to remove irrelevant features before classification. Lasso regression was based on ordinary least squares with L_1 regular expression, where the L_1 regular expression was used to prevent overfitting of models. Lasso can transform the value of irrelevant features into 0, thereby performing feature reduction and selecting important features for classification tasks.

2.6. Classification and validation

After feature selection, generalization of the selected features was evaluated by using four different classification models. Specifically, the Logistic Regression (LR) is simple and easy to implement, yet it has a limited capability to capture complex non-linear relationships. The AdaBoost (AB) can significantly improve model performance by combining weak classifiers, but it is sensitive to noisy data and outliers. The Support Vector Machine (SVM) effectively handles non-linear problems by utilizing kernel tricks, although the selection of an appropriate kernel and parameter tuning can pose challenges. The Random Forest (RF) offers strong robustness and is less prone to overfitting, but

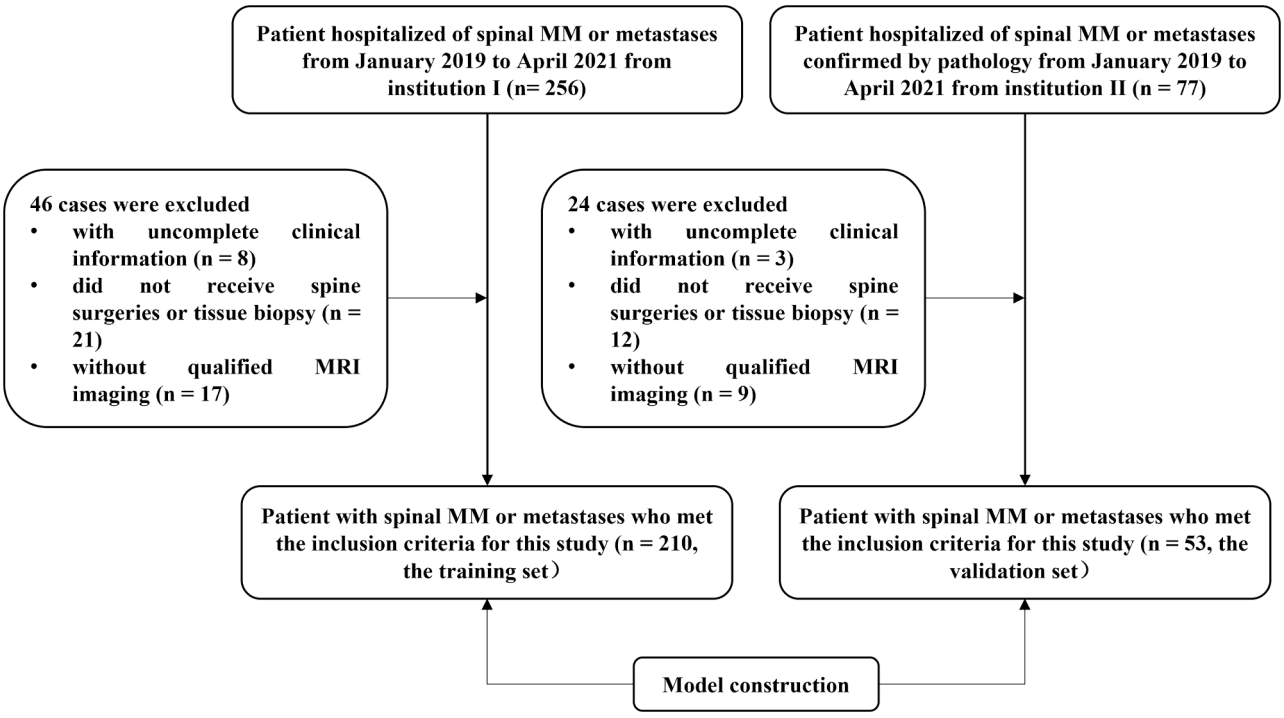

Fig. 1. The flow chart of patient enrolment.

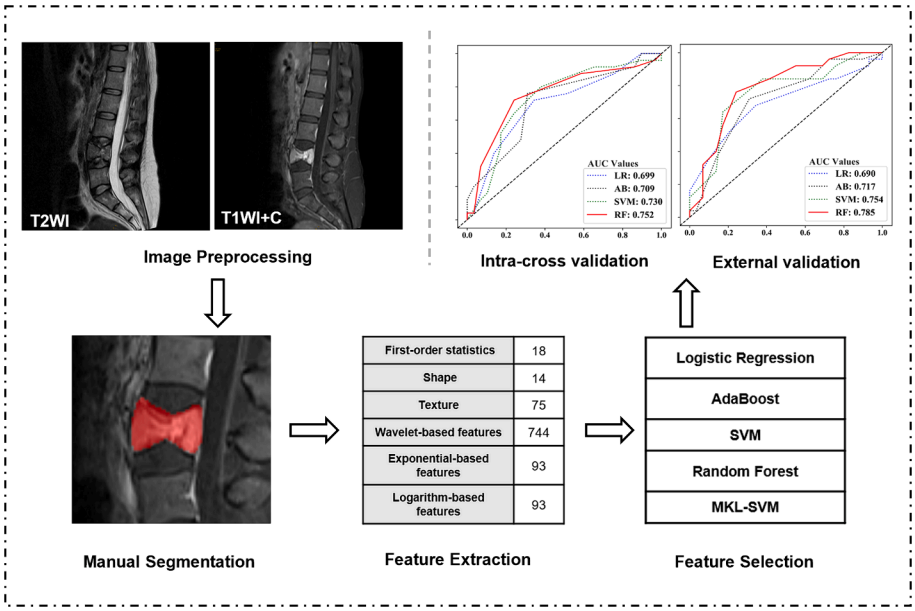

Fig. 2. The radiomics workflow.

may not be suitable for certain types of data, such as sparse data. In addition, to combine the CET1 and T2WI sequences, we first concatenate the features extracted from the CET1 and T2WI images, and then the new features are fed into these classifiers to generate the final results. These classifiers were all imported from a Python (version 3.6.5) machine learning library named scikit-learn (version 20.3). In addition, to combine the CET1 and T2WI sequences, we first concatenate the features extracted from the CET1 and T2WI images, and then the new features are fed into these classifiers to generate the final results.

Additionally, we utilized the multi-kernel learning based SVM (MKL-SVM) algorithm, which combines SVM with multi-kernel learning, to effectively incorporate CET1 and T2WI sequences. MKL-SVM can effectively capture intricate data relationships and enhance classification performance. The detailed steps of MKL-SVM are as follows: 1) The ROIs including the lesions are first cropped from CET1 and T2WI images and the representative features are extracted to form single-sequence features; 2) The SVM classifier is then applied to the single-sequence features and the fused kernel features to generate a classifier pool; 3) The MKL algorithm is then applied to this classifier pool to boost these classifiers to generate the final diagnosis result. It is worth noting that the training time and computational costs of MKL-SVM can be substantial when dealing with numerous kernels. Training data set was split into five equally-sized parts, each exhibiting the same class distribution, and then the five-fold cross-validation was used to tune hyper-parameters. To evaluate their performance between spinal MM and metastases in differential diagnostic models, Accuracy (ACC), Sensitivity (SEN), Specificity (SPE), the area under the ROC curve (AUC), YI, Positive Predictive Value (PPV), Negative Predictive Value (NPY) and F1-score were selected as the metrics.

$$ACC = (TP + TN)/(FP + FN + TN + FP)$$

$$\begin{cases} SEN = TP/(TP + FN) \\ SPE = TN/(TN + FP) \\ YI = SEN + SPE - 1 \\ PPV = TP/(TP + FP) \\ NPV = TN/(TN + FN) \end{cases}$$

$$F1 = 2TP/(2TP + FP + FN)$$

where FN, TN, TP and FP represent false negative, true negative, true positive and false positive, respectively. The overall workflow for radiomics model development is shown in Fig. 2.

2.7. ComBat compensation method

The ComBat compensation method can eliminate batch effects caused by many sources of variability generated by different scanners and protocols while keeping the outperforming features seen in multi-center radiomic investigations. It has been used to increase reproducibility between centers [19].

2.8. Statistical analysis

Statistical tests were implemented using R statistical software (version 3.3.0, https://www.r-project.org). Independent samples *t*-test or MannWhitney *U* test was used to compare continuous variables, and the chi-square test or Fisher test was applied for the categorical variables between the two cohorts. A *P* value smaller than 0.05 was considered statistically significant in this study.

3. Results

Enrolled in this study were 263 patients with pathologically confirmed spinal tumors, including 127 patients with MM and 136 with metastases. A total of 210 of them were form institution I, and the other 53 were from Institution II (Table 1). Distribution of tumor origin for patients with spinal metastases included: lung (n = 72), breast (n = 14), liver (n = 22), kidney (n = 24), and digestive tract (n = 4) (Fig. 3).

Table 2 presents the classification results of different radiomics models based on single-sequence in the training set and external validation sets. Among all models based on CET1 alone and T2 alone, the classification performance of RF outperformed that of LR, AdaBoost, and SVM in both the training and external validation sets. In addition, all models constructed on T2WI were found to be superior to those based on CET1 with higher values of ACC and AUC in both the training set (0.819 and 0.834 of RF *vs.* 0.782 and 0.806 of SVM *vs.* 0.760 and 0.756 of AdaBoost *vs.* 0.730 and 0.739 of LR) and the external validation set (0.759 and 0.785 of RF *vs.* 0.741 and 0.754 of SVM *vs.* 0.704 and 0.717 of AdaBoost *vs.* 0.667 and 0.690 of LR). The ROC curves for all radiomics models based on single-sequence are shown in Fig. 4. It can be observed that the performance of all models was generally stable, and RF achieved

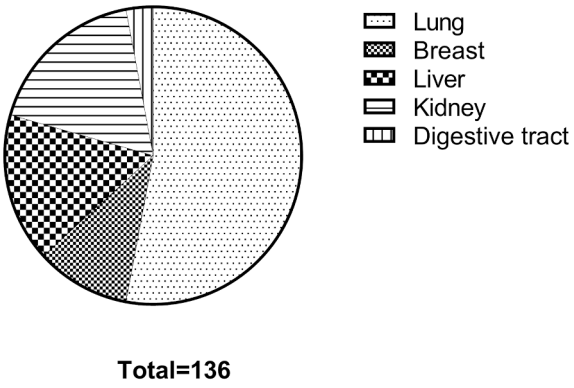

Fig. 3. The pie chart of distribution of tumor origin for patients with spinal metastases.

better performance than the other models. In addition, radiomics classifiers based on incorporation of CET1 with T2WI sequences performed better than their respective counterparts based on CETI or T2WI images alone (Table 3 **and** Fig. 5). The MKL-SVM model achieved optimal performance with an ACC of 0.862 and AUC 0.870, followed by RF (0.853 and 0.865), SVM (0.823 and 0.833), AdaBoost (0.791 and 0.793), and LR (0.752 and 0.788).

4. Discussion

In this two-center study, we constructed MRI-based radiomics models to differentiate spinal MM from metastases. In all radiomics models based on single-sequence, RF showed a stronger capability in classification than LR, AdaBoost, and SVM. In addition, radiomics models from T2WI achieved better performance than those based on CET1. Moreover, our research has illustrated the value of radiomics classifiers from joint T2WI with CET1 in differentiating spinal malignant tumors. The MKL-SVM model yielded the highest ACC and AUC among all models. In brief, the methodology developed in this study could serve as a reliable tool for differentiation between spinal MM and metastases. To the best of our knowledge, this research is the first multicenter study that applied radiomics method to differentiate spinal MM from metastases.

With the arrival of the era of precision medicine, individualized diagnosis and treatment plays a pivotal role in the management of cancer patients. Given huge differences between spinal MM and metastases, timely and accurate diagnosis is crucial for choosing the most appropriate therapies [20,21]. Although needle biopsy serves as the "gold standard" of diagnosis for spinal MM and metastases, its clinical application is limited by its invasiveness and potential false negative rates. Being non-invasive, imaging examination plays an essential role in pretreatment evaluation and efficacy assessment. However, both spinal MM and metastases imageologically present as a single lesion or multiple lytic lesions, which makes the differential diagnosis between them extremely challenging and to some extent limits the efficacy of differential diagnosis by conventional imaging examinations such as X-ray, CT, and MRI [3,4,22]. Prior studies have pointed out that advanced MRI methods are useful in differential diagnosis between spinal MM and metastases. Lang et al. [23] reported the application of dynamic contrast-enhanced MRI (DCE-MRI) in differentiating spinal MM and metastases, which could provide additional information that conventional MRI could not obtain to differentiate MM from metastases. Similar conclusions have been also reached in other studies [24–26]. Park et al. [4] and Hwang et al. [27] reported that MR combined with diffusion-weighted imaging (DWI) could help distinguish MM from metastases in the spine and extremities. Nevertheless, not all medical conditions are equipped with advanced imaging devices, requiring sophisticated acquisition and analysis methods. Therefore, it is more practical and

Table 2
Classification results of different radiomics models constructed by single-sequence in the training and external validation sets.

MR sequence	Models	Training set (Institution I)								External validation set (Institution II)							
		ACC	SEN	SPE	YI	PPV	NPV	F1	AUC	ACC	SEN	SPE	YI	PPV	NPV	F1	AUC
CET1	LR	0.710	0.792	0.616	0.408	0.699	0.728	0.742	0.701	0.685	0.720	0.655	0.375	0.643	0.731	0.679	0.699
	AdaBoost	0.743	0.820	0.657	0.477	0.730	0.765	0.771	0.718	0.704	0.640	0.759	0.399	0.696	0.710	0.667	0.709
	SVM	0.761	0.829	0.684	0.513	0.750	0.779	0.787	0.756	0.722	0.760	0.690	0.450	0.679	0.769	0.717	0.730
	RF	0.818	0.856	0.775	0.631	0.812	0.828	0.833	0.822	0.741	0.720	0.759	0.479	0.720	0.759	0.720	0.752
T2	LR	0.730	0.821	0.637	0.447	0.715	0.763	0.762	0.739	0.667	0.680	0.655	0.335	0.630	0.704	0.654	0.690
	AdaBoost	0.760	0.804	0.710	0.514	0.757	0.766	0.779	0.756	0.704	0.720	0.690	0.410	0.667	0.741	0.692	0.717
	SVM	0.782	0.874	0.680	0.554	0.754	0.835	0.808	0.806	0.741	0.640	0.828	0.468	0.762	0.727	0.696	0.754
	RF	0.819	0.919	0.707	0.625	0.779	0.887	0.843	0.834	0.759	0.760	0.759	0.519	0.731	0.786	0.745	0.785

ACC, accuracy; SEN, sensitivity; SPE, specificity; YI, Youden index; PPV, positive predictive value; NPV, negative predictive value; AUC, the area under the receiver operating characteristic (ROC) curve.

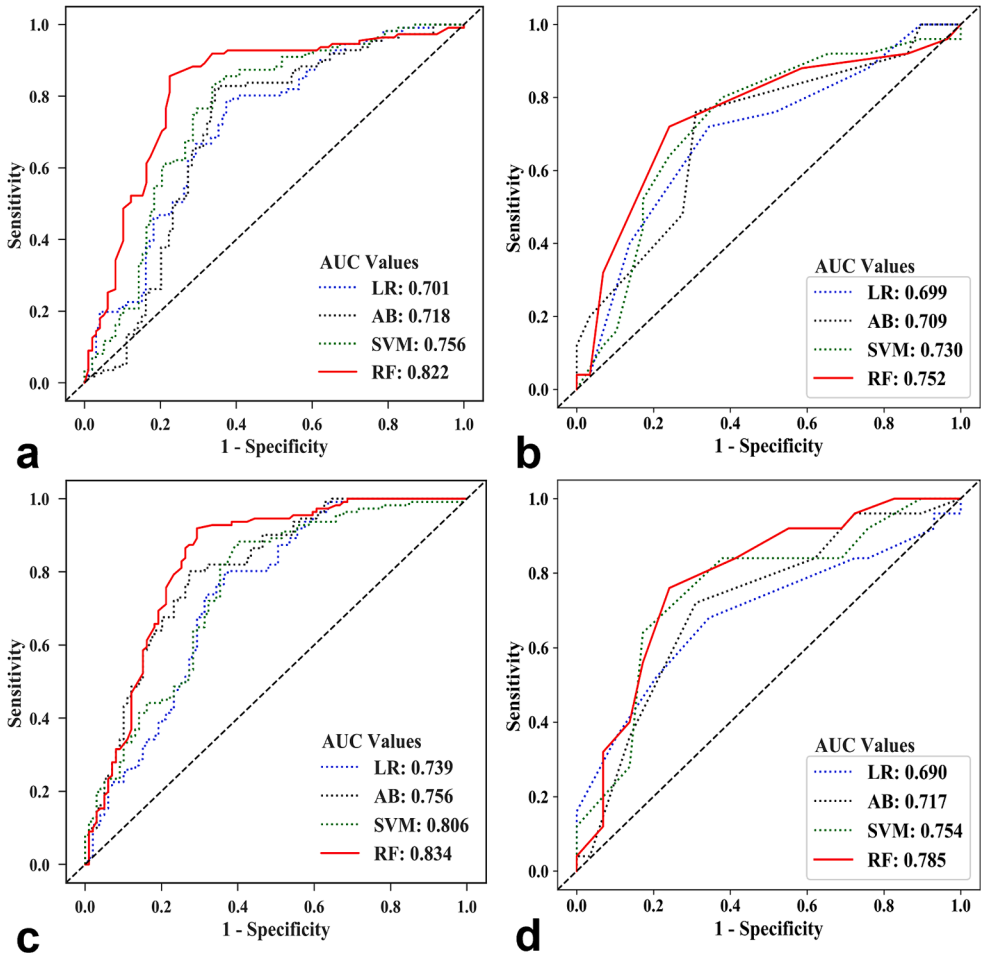

Fig. 4. ROC curves of different radiomics models based on CET1 alone in the training set (a) and the validation set (b), and T2WI alone in the training set (c) and the validation set (d).

Table 3
Classification results of different radiomics models based on incorporation of CET1 and T2 sequences in the training set.

Models	ACC	SEN	SPE	YI	PPV	NPV	F1	AUC
LR	0.752	0.811	0.687	0.498	0.744	0.764	0.776	0.788
AdaBoost	0.791	0.811	0.768	0.579	0.798	0.784	0.804	0.793
SVM	0.823	0.900	0.737	0.637	0.794	0.873	0.843	0.833
RF	0.853	0.847	0.860	0.707	0.874	0.836	0.859	0.865
MKL-SVM	0.862	0.910	0.808	0.717	0.841	0.893	0.874	0.870

ACC, accuracy; SEN, sensitivity; SPE, specificity; YI, Youden index; PPV, positive predictive value; NPV, negative predictive value; AUC, the area under the receiver operating characteristic (ROC) curve.

preferred for clinical work-up to classify spinal tumors based on conventional MRI sequences. Additionally, both conventional and advanced MRI tend to be impacted by the experience of radiologists, and they lack objectivity and quantification to some extent [19].

Radiomics could provide an objective assessment of tissue heterogeneity and lesion heterogeneity, thereby providing a new method to collect information about the microenvironment of lesions that is impossible to observe visually. Over the past several years, radiomics analysis has become a common approach for gathering information from medical images to perform a variety of clinical tasks, such as differentiating benign and malignant tumors and predicting therapeutic outcomes or prognoses [3,7,28–30]. So far, only sporadic reports have demonstrated the efficiency of radiomics analysis in differentiating spinal MM from metastases. Jin et al. [31] constructed radiomics model based on ^{18}F-FDG PET/CT images and achieved excellent diagnostic performance for differentiation between MM and bone metastases, and the optimal model achieved an AUC value of 0.973. Although ^{18}F-FDG PET/CT is recommended as one of the optimal imaging examinations, its high radiation exposure and high cost are problems that need to be solved, especially in developing countries.

As one of the most widely used imaging modalities, MRI has proved to be effective in radiomics analysis for classifying spinal MM from metastases [1,3]. Xiong et al. reported that compared with SVM, K-Nearest Neighbor (KNN), RF, and Naïve Bayes (NB), the, Artificial Neural Networks (ANN) exhibited the best performance in differentiating lumbar MM from metastasis based on T2WI images with accuracy, sensitivity, and specificity of 0.815, 0.879, and 0.790, respectively [3]. They also found that T2WI sequences contained more valuable texture features than T1WI for differentiating MM from metastases. Unlike their study based on 10-fold cross-validation, Liu et al. constructed radiomics models with an appropriate small number of the most frequent features using ten times 5-fold cross-validation and demonstrated its efficiency of

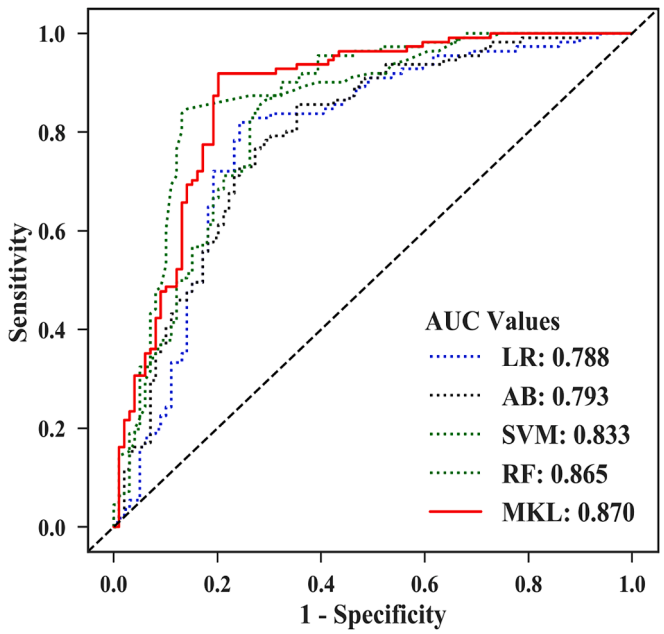

Fig. 5. ROC curves of different radiomics models based on the incorporation of CET1 and T2WI sequences in the training set.

differentiating MM from metastasis based on conventional vertebral MRI [1]. The 10 EPV-Model in their study achieved optimal performance with AUC of 0.84. Moderate efficiency was achieved by radiomics models in the two studies mentioned above, which are consistent with our findings. In addition, their studies were carried out in one institute without an external validation set. In our study, we enrolled more patients from two institutes and validated the efficiency of models in an external validation set.

In this study, we trained and validated classifiers by using machine-learning algorithms including LR, AdaBoost, SVM, RF, and MKL-SVM. Unlike Xiong et al. and Liu et al., we constructed radiomics models based on the sequences of T2WI alone, CET1 alone, and both. Because radiologists usually rely on CET1 to make diagnosis by human eyes, which can depict vascularity of the lesions, reflect the degree of malignancy, and distinguish necroses and solid tumors. Whereas T2WI could effectively depict the lesion boundaries and reveal the overall density of lesions to a certain extent. Our results show that all models based on T2WI images performed better than those based on CET1. The findings of our study are consistent with other radiomics studies based on MRI or CT in that models constructed from non-contrast sequences were superior to those based on enhanced sequences [32,33]. The underlying reason may be that contrast enhancement could interfere with the true grayscale, uniformity, contrast, texture depth, and depth thickness in radiomics, which may then lead to poor performance in differentiating different tumors because of the existing intra-tumoral contrast material [33,34]. Among all radiomics models constructed based on single-sequence, the RF model achieved the best performance for differential diagnosis from both T2WI and CET1 in this study. By incorporating CET1 and T2WI sequences, the efficiency of all models was boosted and the MKL model achieved the best performance with an ACC, AUC, and F1-score of 0.86, 0.87, and 0.87, respectively (Table 3 and Fig. 5). Our results indicated that compared with the tandem strategy in other radiomic models, the MKL-SVM algorithm with a linear convex combination of polynomial kernel and sigmoid kernel could effectively fuse bimodal data with better performance in differential diagnosis. The MKL has been demonstrated to improve classification accuracy and robustness [35]. It is impossible to construct a universal optimal learning algorithm in all fields. Nevertheless, the classifiers constructed in our study showed capability of RF and MKL-SVM in distinguishing spinal MM from metastases with satisfied performance.

There are several limitations in our study. First, since the images were reviewed retrospectively, the possibility of selection bias is unavoidable despite our stringent criteria. Second, manual tumor segmentation may lead to subjectivity and irregularities. Third, although the experimental data were from two institutions, the differences in MRI scanners and protocols still existed to some extent. To lessen the disparities in picture specifications, we used resampling methodology and the ComBat compensation method, with the goal of increasing the stability of features and different models. Finally, as it is less realistic to include all types of spinal metastases, we only selected several common types of spinal metastases as the metastatic group in this study. Therefore, larger-sample studies are required to increase model generalization. With the sample size increasing, we will further classify different subtypes of spinal metastases.

5. Conclusion

Our findings demonstrate the satisfactory performance of radiomics models based on conventional MRI sequences to differentiate spinal MM from metastases. Machine learning classifiers could potentially be valuable tools for optimizing precision medicine applied to spinal tumors.

Funding

The work was supported by the National Natural Science Foundation of China (Grant No. 82001812 and 81930049), and Special Project for Promoting High-Quality Development of Industries in Shanghai, 2022-2023 (Artificial Intelligence Topic, Grant No. 2023-GZL-RGZN-01014).

CRediT authorship contribution statement

Jiashi Cao: Writing – original draft, Writing – review & editing. **Qiong Li:** Data curation, Investigation. **Huili Zhang:** Investigation, Methodology, Writing – review & editing. **Yanyan Wu:** Investigation. **Xiang Wang:** Data curation. **Saisai Ding:** Methodology. **Song Chen:** Data curation. **Shaochun Xu:** Data curation. **Guangwen Duan:** Data curation. **Defu Qiu:** Methodology, Software. **Jiuyi Sun:** Conceptualization, Project administration. **Jun Shi:** Supervision, Writing – review & editing. **Shiyuan Liu:** Conceptualization, Project administration.

Declaration of Competing Interest

The authors declare that they have no known competing financial interests or personal relationships that could have appeared to influence the work reported in this paper.

Acknowledgements

Our deepest gratitude goes to all the patients with spinal MM and metastases enrolled in this study. We also thank Prof. Shunxing Zhang for language assistance when revising the manuscript.

References

[1] J. Liu, W. Guo, P. Zeng, Y. Geng, Y. Liu, H. Ouyang, N. Lang, H. Yuan, Vertebral MRI-based radiomics model to differentiate multiple myeloma from metastases: influence of features number on logistic regression model performance, Eur. Radiol. 32 (1) (2022) 572–581.
[2] A. Amelot, A. Moles, J. Cristini, C. Salaud, C. Touzeau, O. Hamel, E. Bord, K. Buffenoir, Predictors of survival in patients with surgical spine multiple myeloma metastases, Surg. Oncol. 25 (3) (2016) 178–183.
[3] X. Xiong, J. Wang, S. Hu, Y. Dai, Y. Zhang, C. Hu, Differentiating between multiple myeloma and metastasis subtypes of lumbar vertebra lesions using machine learning-based radiomics, Front. Oncol. 11 (2021) 601699.
[4] G.E. Park, W.-H. Jee, S.-Y. Lee, J.-K. Sung, J.-Y. Jung, R. Grimm, Y. Son, M.Y. Paek, C.-K. Min, K.-Y. Ha, J.H. Sherman, Differentiation of multiple myeloma and

metastases: use of axial diffusion-weighted MR imaging in addition to standard MR imaging at 3T, PLoS One 13 (12) (2018) e0208860.
[5] X. Xing, J. Zhang, Y. Chen, Q. Zhao, N. Lang, H. Yuan, Application of monoexponential, biexponential, and stretched-exponential models of diffusion-weighted magnetic resonance imaging in the differential diagnosis of metastases and myeloma in the spine-Univariate and multivariate analysis of related parameters, Br. J. Radiol. 93 (1112) (2020) 20190891.
[6] K. Ekert, C. Hinterleitner, K. Baumgartner, J. Fritz, M. Horger, Extended texture analysis of non-enhanced whole-body MRI image data for response assessment in multiple myeloma patients undergoing systemic therapy, Cancers (Basel) 12 (3) (2020) 761.
[7] N. Lang, Y. Zhang, E. Zhang, J. Zhang, D. Chow, P. Chang, H.J. Yu, H. Yuan, M. Y. Su, Differentiation of spinal metastases originated from lung and other cancers using radiomics and deep learning based on DCE-MRI, Magn. Reson. Imaging 64 (2019) 4–12.
[8] A. Piccioli, G. Maccauro, M.S. Spinelli, R. Biagini, B. Rossi, Bone metastases of unknown origin: epidemiology and principles of management, J. Orthop. Traumatol. 16 (2) (2015) 81–86.
[9] D.M. Sciubba, R.J. Petteys, M.B. Dekutoski, C.G. Fisher, M.G. Fehlings, S.L. Ondra, L.D. Rhines, Z.L. Gokaslan, Diagnosis and management of metastatic spine disease. A review, J. Neurosurg. Spine 13 (1) (2010) 94–108.
[10] D.T. Cawley, J.S. Butler, A. Benton, F. Altaf, K. Rezajooi, C. Kyriakou, S. Selvadurai, S. Molloy, Managing the cervical spine in multiple myeloma patients, Hematol. Oncol. 37 (2) (2019) 129–135.
[11] M. Yildirim, M. Baykara, Differentiation of multiple myeloma and lytic bone metastases: histogram analysis, J. Comput. Assist. Tomogr. 44 (6) (2020) 953–955.
[12] H.J. Kim, K.N. Ryu, W.S. Choi, B.K. Choi, J.M. Choi, Y. Yoon, Spinal involvement of hematopoietic malignancies and metastasis: differentiation using MR imaging, Clin. Imaging 23 (2) (1999) 125–133.
[13] Y.H. Baek, H.L. Jeon, I.S. Oh, H. Yang, J. Park, J.Y. Shin, Incidence of skeletal-related events in patients with breast or prostate cancer-induced bone metastasis or multiple myeloma: a 12-year longitudinal nationwide healthcare database study, Cancer Epidemiol. 61 (2019) 104–110.
[14] P. Yin, N. Mao, C. Zhao, J. Wu, C. Sun, L. Chen, N. Hong, Comparison of radiomics machine-learning classifiers and feature selection for differentiation of sacral chordoma and sacral giant cell tumour based on 3D computed tomography features, Eur. Radiol. 29 (4) (2019) 1841–1847.
[15] X. Wang, X. Zhao, Q. Li, W. Xia, Z. Peng, R. Zhang, Q. Li, J. Jian, W. Wang, Y. Tang, S. Liu, X. Gao, Can peritumoral radiomics increase the efficiency of the prediction for lymph node metastasis in clinical stage T1 lung adenocarcinoma on CT? Eur. Radiol. 29 (11) (2019) 6049–6058.
[16] A. Conti, A. Duggento, I. Indovina, M. Guerrisi, N. Toschi, Radiomics in breast cancer classification and prediction, Semin. Cancer Biol. 72 (2021) 238–250.
[17] R. Cannella, L. La Grutta, M. Midiri, T.V. Bartolotta, New advances in radiomics of gastrointestinal stromal tumors, World J. Gastroenterol. 26 (32) (2020) 4729–4738.
[18] P.A. Yushkevich, J. Piven, H.C. Hazlett, R.G. Smith, S. Ho, J.C. Gee, G. Gerig, User-guided 3D active contour segmentation of anatomical structures: significantly improved efficiency and reliability, Neuroimage 31 (3) (2006) 1116–1128.
[19] R. Yan, D. Hao, J. Li, J. Liu, F. Hou, H. Chen, L. Duan, C. Huang, H. Wang, T. Yu, Magnetic resonance imaging-based radiomics nomogram for prediction of the histopathological grade of soft tissue sarcomas: a two-center study, J. Magn. Reson. Imaging 53 (6) (2021) 1683–1696.
[20] A. Sahgal, S.D. Myrehaug, S. Siva, G.L. Masucci, P.J. Maralani, M. Brundage, J. Butler, E. Chow, M.G. Fehlings, M. Foote, Z. Gabos, J. Greenspoon, M. Kerba, Y. Lee, M. Liu, S.K. Liu, I. Thibault, R.K. Wong, M. Hum, K. Ding, W.R. Parulekar, i. trial, Stereotactic body radiotherapy versus conventional external beam radiotherapy in patients with painful spinal metastases: an open-label, multicentre, randomised, controlled, phase 2/3 trial, Lancet Oncol. 22 (7) (2021) 1023–1033.
[21] N. van de Donk, C. Pawlyn, K.L. Yong, Multiple myeloma, Lancet 397 (10272) (2021) 410–427.
[22] Y. Shigematsu, T. Hirai, K. Kawanaka, S. Shiraishi, M. Yoshida, M. Kitajima, H. Uetani, M. Azuma, Y. Iryo, Y. Yamashita, Distinguishing imaging features between spinal hyperplastic hematopoietic bone marrow and bone metastasis, AJNR Am. J. Neuroradiol. 35 (10) (2014) 2013–2020.
[23] N. Lang, M.Y. Su, H.J. Yu, M. Lin, M.J. Hamamura, H. Yuan, Differentiation of myeloma and metastatic cancer in the spine using dynamic contrast-enhanced MRI, Magn. Reson. Imaging 31 (8) (2013) 1285–1291.
[24] T. Pearce, S. Philip, J. Brown, D.M. Koh, P.R. Burn, Bone metastases from prostate, breast and multiple myeloma: differences in lesion conspicuity at short-tau inversion recovery and diffusion-weighted MRI, Br. J. Radiol. 85 (1016) (2012) 1102–1106.
[25] A. Saha, K.K. Peck, E. Lis, A.I. Holodny, Y. Yamada, S. Karimi, Magnetic resonance perfusion characteristics of hypervascular renal and hypovascular prostate spinal metastases: clinical utilities and implications, Spine (Phila Pa 1976) 39 (24) (2014) E1433–E1440.
[26] N.R. Khadem, S. Karimi, K.K. Peck, Y. Yamada, E. Lis, J. Lyo, M. Bilsky, H. A. Vargas, A.I. Holodny, Characterizing hypervascular and hypovascular metastases and normal bone marrow of the spine using dynamic contrast-enhanced MR imaging, AJNR Am. J. Neuroradiol. 33 (11) (2012) 2178–2185.
[27] H. Hwang, S.K. Lee, J.Y. Kim, Comparison of conventional magnetic resonance imaging and diffusion-weighted imaging in the differentiation of bone plasmacytoma from bone metastasis in the extremities, Diagn. Interv. Imaging 102 (10) (2021) 611–618.
[28] H.J. Aerts, E.R. Velazquez, R.T. Leijenaar, C. Parmar, P. Grossmann, S. Carvalho, J. Bussink, R. Monshouwer, B. Haibe-Kains, D. Rietveld, F. Hoebers, M. M. Rietbergen, C.R. Leemans, A. Dekker, J. Quackenbush, R.J. Gillies, P. Lambin, Decoding tumour phenotype by noninvasive imaging using a quantitative radiomics approach, Nat. Commun. 5 (2014) 4006.
[29] N.M. Braman, M. Etesami, P. Prasanna, C. Dubchuk, H. Gilmore, P. Tiwari, D. Plecha, A. Madabhushi, Intratumoral and peritumoral radiomics for the pretreatment prediction of pathological complete response to neoadjuvant chemotherapy based on breast DCE-MRI, Breast Cancer Res. 19 (1) (2017) 57.
[30] G. Wang, L. He, C. Yuan, Y. Huang, Z. Liu, C. Liang, Pretreatment MR imaging radiomics signatures for response prediction to induction chemotherapy in patients with nasopharyngeal carcinoma, Eur. J. Radiol. 98 (2018) 100–106.
[31] Z. Jin, Y. Wang, Y. Wang, Y. Mao, F. Zhang, J. Yu, Application of 18F-FDG PET-CT images based radiomics in identifying vertebral multiple myeloma and bone metastases, Front. Med. (Lausanne) 9 (2022) 874847.
[32] Y. Dai, P. Yin, N. Mao, C. Sun, J. Wu, G. Cheng, N. Hong, Differentiation of pelvic osteosarcoma and ewing sarcoma using radiomic analysis based on T2-weighted images and contrast-enhanced T1-weighted images, Biomed Res. Int. 2020 (2020) 9078603.
[33] L. He, Y. Huang, Z. Ma, C. Liang, C. Liang, Z. Liu, Effects of contrast-enhancement, reconstruction slice thickness and convolution kernel on the diagnostic performance of radiomics signature in solitary pulmonary nodule, Sci. Rep. 6 (2016) 34921.
[34] Y. Han, T. Wang, P. Wu, H. Zhang, H. Chen, C. Yang, Meningiomas: preoperative predictive histopathological grading based on radiomics of MRI, Magn. Reson. Imaging 77 (2021) 36–43.
[35] J. Chang, Y. Li, H. Zheng, Research on key algorithms of the lung CAD system based on cascade feature and hybrid swarm intelligence optimization for MKL-SVM, Comput. Intell. Neurosci. 2021 (2021) 5491017.